Bioactive Materials 6 (2021) 1423–1435

Contents lists available at ScienceDirect

Bioactive Materials

journal homepage: www.sciencedirect.com/journal/bioactive-materials

Sialic acid-engineered mesoporous polydopamine nanoparticles loaded with SPIO and Fe^{3+} as a novel theranostic agent for T1/T2 dual-mode MRI-guided combined chemo-photothermal treatment of hepatic cancer

Gaofeng Shu [a,b,1], Minjiang Chen [a,1], Jingjing Song [a,1], Xiaoling Xu [b], Chenying Lu [a], Yuyin Du [c], Min Xu [a], Zhongwei Zhao [a], Minxia Zhu [b], Kai Fan [a], Xiaoxi Fan [a], Shiji Fang [a], Bufu Tang [a], Yiyang Dai [d], Yongzhong Du [b,**], Jiansong Ji [a,*]

[a] Key Laboratory of Imaging Diagnosis and Minimally Invasive Intervention Research, Lishui Hospital of Zhejiang University, School of Medicine, Lishui, Zhejiang, 323000, China
[b] Institute of Pharmaceutics, College of Pharmaceutical Sciences, Zhejiang University, Hangzhou, 310058, PR China
[c] Department of Chemistry, Faculty of Science, Tohoku University, Sendai, 980-8577, Japan
[d] Department of Gastroenterology, The Fourth Affiliated Hospital of Zhejiang University, School of Medicine, 32200, YiWu, China

ARTICLE INFO

Keywords:
Hepatic cancer
Mesoporous polydopamine
Chemo-photothermal combined therapy
T1/T2 dual-mode MRI
Targeted delivery

ABSTRACT

Hepatic cancer is a serious disease with high morbidity and mortality. Theranostic agents with effective diagnostic and therapeutic capability are highly needed for the treatment of hepatic cancer. Herein, we aimed to develop a novel mesoporous polydopamine (MPDA)-based theranostic agent for T1/T2 dual magnetic resonance imaging (MRI)-guided cancer chemo-photothermal therapy. Superparamagnetic iron oxide (SPIO)-loaded MPDA NPs (MPDA@SPIO) was firstly prepared, followed by modifying with a targeted molecule of sialic acid (SA) and chelating with Fe^{3+} (SA-MPDA@SPIO/Fe^{3+} NPs). After that, doxorubicin (DOX)-loaded SA-MPDA@SPIO/Fe^{3+} NPs (SA-MPDA@SPIO/DOX/Fe^{3+}) was prepared for tumor theranostics. The prepared SAPEG-MPDA@SPIO/Fe^{3+} NPs were water-dispersible and biocompatible as evidenced by MTT assay. *In vitro* photothermal and relaxivity property suggested that the novel theranostic agent possessed excellent photothermal conversion capability and photostability, with relaxivity of being $r_1 = 4.29\ mM^{-1}s^{-1}$ and $r_2 = 105.53\ mM^{-1}s^{-1}$, respectively. SAPEG-MPDA@SPIO/Fe^{3+} NPs could effectively encapsulate the DOX, showing dual pH- and thermal-triggered drug release behavior. *In vitro* and *in vivo* studies revealed that SA-MPDA@SPIO/DOX/Fe^{3+} NPs could effectively target to the hepatic tumor tissue, which was possibly due to the specific interaction between SA and the overexpressed E-selectin. This behavior also endowed SA-MPDA@SPIO/DOX/Fe^{3+} NPs with a more precise T1-T2 dual mode contrast imaging effect than the one without SA modification. In addition, SAPEG-MPDA@SPIO/DOX/Fe^{3+} NPs displayed a superior therapeutic effect, which was due to its active targeting ability and combined effects of chemotherapy and photothermal therapy. These results demonstrated that SAPEG-MPDA@SPIO/DOX/Fe^{3+} NPs is an effective targeted nanoplatform for tumor theranostics, having potential value in the effective treatment of hepatic cancer.

1. Introduction

Liver cancer is considered to be one of the most common cancers, which is the third leading cause of cancer-related death in the word [1,2]. Unfortunately, most of patients with liver cancer are diagnosed at advanced stages, thereby resulting in limited treatment options. Currently, chemotherapy is still an important strategy for clinical treatment of liver cancer. However, the traditional chemotherapy is still facing challenges due to that the chemotherapeutic drugs cannot distinguish the normal and cancer cells, thereby causing serious damages to the normal tissues [3,4]. In addition, the personalized treatment of cancer by chemotherapeutic drugs cannot be achieved, which is due

* Corresponding author. Department of Radiology, Lishui Hospital of Zhejiang University, China.
** Corresponding author. Institute of Pharmaceutics, College of Pharmaceutical Sciences, Zhejiang University, 866 Yu-Hang-Tang Road, Hangzhou, 310058, China.
E-mail addresses: duyongzhong@zju.edu.cn (Y. Du), lschrjjs@163.com (J. Ji).
[1] These authors contributed equally to this work.

https://doi.org/10.1016/j.bioactmat.2020.10.020
Received 30 June 2020; Received in revised form 26 October 2020; Accepted 26 October 2020

to that it is extremely hard to trace the distribution of drugs in the tumor tissue, thus having no ability to provide timely feedback in clinic [5]. A promising method for addressing aforementioned difficulties is to use the theranostic nanomedicines, which simultaneously integrates the diagnostic and therapeutic agents into one single nanoplatform [6].

Magnetic resonance imaging (MRI) is known to be a dominant tool for the diagnose of tumors because of the noninvasiveness, superior resolution in soft tissue, and non-limited penetration depth [7,8]. For more accurate diagnosis, contrast agents are commonly used to enhance the imaging contrast between the biological targets and the surrounding tissues [9]. By now, the commercially available contrast agents of MRI are categorized into two forms: the T1 positive and T2 negative contrast agents. T1 positive contrast agents, such as gadolinium (Gd)-based chelates, are able to accelerate the longitudinal relaxation rate, thus producing a brighter signal in T1 images [10]. T2 negative contrast agents, such as superparamagnetic iron oxide (SPIO) nanoparticles, can facilitate the transverse relaxation rate, thereby providing a darker signal in T2 images [11].

Nevertheless, the use of a single-mode contrast agent is still facing deficiencies, especially in the precise detection of tumors with small areas. The Gd-based T1 contrast agents have a short blood circulation time, making it difficult to acquire images with high resolution [12]. Besides, Gd-based contrast agents may result in potential risks of adverse reactions, such as nephrogenic systemic fibrosis [13]. The clinical applications of T2 contrast agents are not yet preferred, which is related to their negative contrast effect and susceptibility artifacts [14]. One effective approach to overcome aforementioned challenges is to apply the T1/T2 dual-mode contrast agents, which could offer complementary diagnostic images with less false errors [15,16]. In this regard, the utilization of theranostic agents with dual T1 and T2 weighted MRI functions is a highly positive strategy for effective treatment of cancers.

Photothermal therapy (PTT) is a noninvasive technique for the treatment of different types of cancers. It is based on the photoabsorbers that can convert the light energy into thermal energy, thereby ablating the cancer cells by the cytotoxic heat. However, the utilization of PTT alone for cancer treatment is also facing some problems [17]: (i) complete cancer ablation by photothermal treatment is difficult, which is due to the uneven heat production caused by the heterogeneous distribution of nanoparticles and the Gaussian distribution of laser beam energy; (ii) the laser energy gradually reduces after penetrating into the tissue, often resulting in insufficient effect deep inside the tumors.

In order to improve the anticancer efficacy, the combined nanomaterial-based chemo-photothermal therapy is widely used, which has superior therapeutic outcomes than the two treatments alone due to the additive or synergistic effect [18]. By using chemo-photothermal therapy, the released chemotherapeutic drugs could kill the cancer cells outside the laser path, therefore overcoming the limitation associated with PTT. On the other hand, as compared with chemotherapy, the combined chemo-photothermal therapy can achieve similar anticancer effect by using a much lower level of chemotherapeutic drugs, thus considerably reducing the side effects. Thus, the development of theranostic agents having combined chemo-photothermal therapy is also a satisfactory approach for effective treatment of cancers. Currently, the commonly used photothermal agents are inorganic nanomaterials, including copper sulfide nanoparticles [19], carbon-based nanomaterials [20], and various gold nanostructures [21]. However, the utilization of these nanomaterials for cancer theranostics still face problems, which is due to that they may lead to long-term toxicity in their further clinical implementation.

Polydopamine (PDA) as an emerging photothermal agent has attracted a growing attention due to its good biodegradability, no long-term toxicity, easy surface modification, and high photothermal conversion efficiency [22]. In addition, it is widely published that PDA-based materials are also advantageous platforms for preparing MRI contrast agents. For example, previous studies have found that PDA-coated SPIO (PDA@SPIO) NPs have a considerably enhanced T2 weighted MR contrast compared with the individual SPIO NPs, which is associated with the high degree of aggregation of the SPIO magnetic NPs cores [23]. Moreover, PDA could provide anchoring sites for various metal ions owing to its excellent coordination capability. Among them, the PDA NPs complexed with Fe^{3+}, Gd^{3+}, or Mn^{2+} ions have been evidenced as T1 MRI contrast agents [24,25]. In addition, Chen et al., reported a PDA-based coordination nanocomplex for T1/T2 dual mode MRI-guided cancer synergistic therapy [26]. Compared with PDA, mesoporous polydopamine (MPDA) NPs with mesoporous structures and larger surface areas have significant advantages, which exhibit a higher drug loading capability and photothermal conversion efficiency, which may result in enhanced therapeutic effectiveness and reduced side effects [27,28]. However, to our best knowledge, MPDA-based theranostic agent having T1/T2 dual model MRI-guided chemo--photothermal therapy is not reported yet.

The fabrication of theranostics with active targeting ability is also a hot topic in recent years, due to their enhanced imaging sensitivity, improved antitumor efficacy, and reduced systemic side effects [4,29]. E-selectin as a transmembrane glycoprotein that is found to be highly upregulated on the surfaces of inflammatory vascular endothelial cells (VECs) and tumor cells [30–32]. Sialic acid (SA) is a 9-carbon monosaccharide that has specific ability to bind with E-selectin, which is frequently used as a targeted molecule to modify the nanomedicine for the treatment of inflammatory-related diseases and cancers [33,34]. Our previous study also has showed that SA-modified polymeric micelles could effectively target the inflammatory VECs in the tumor site, followed by selectively internalized into tumor cells, which can significantly improve the anticancer efficacy and reduce the side effect [35]. Thus, MPDA-based theranostics modified with SA could be a potent nanoplatform for targeted therapy of liver cancer.

Herein, we fabricated a SA-modified Fe^{3+}-chelated MPDA-capped SPIO nanoparticles (SA-MPDA@SPIO/Fe^{3+} NPs), which could effectively encapsulate the chemotherapy drug (DOX) for T1/T2 dual modal MRI-guided targeted chemophothermal therapy of liver cancer. The surface modification of SA could endow the DOX-loaded SA-MPDA@SPIO/Fe^{3+} NPs with high targeting ability to accumulate in the tumor tissues via the high affinity of SA with the E-selectin overexpressed in tumor. The DOX-loaded SAPEG-MPDA@SPIO/Fe^{3+} had a prominent anticancer efficacy due to the combined effect of chemotherapy and PTT Moreover, the chelation of Fe^{3+} and encapsulation of SPIO endows the MPDA NPs with T_1/T_2 dual model MRI-guided therapy in an effective and safe way.

2. Materials and methods

2.1. Materials

Iron acetylacetonate ($Fe(acac)_3$), 1,2-dodecanediol , oleic acid (OA) , oleyamine (OLA), dopamine hydrochloride, ammonia (NH3·H2O, 25–28%), and doxorubicin hydrochloride (DOX) were purchased from Aladdin Bio-Chem Technology Co. Limited (Shanghai, China). Anti-CD62E (E-selectin) antibodies were purchased from Abcam (UK). Sialic acid (SA) was purchased from Dalian Meilun Biotechnology Co., Ltd (Dalian, China). NH_2-PEG-NH_2 (Mw = 5000) was bought from shanghai Seebio Biotech Co., Ltd. Pluronic F127, Pluronic 123, 1,3,5-trimethylbenzene (TMB), tetrazolium (MTT), and indocyanine green dye (ICG) were purchased from Sigma Chemical Co. (St. Louis, MO). All other chemicals used in the current work were of analytical or chromatographic grades.

2.2. Preparation of OA-stabilized SPIO NPs

OA-stabilized SPIO NPs were synthesized by a thermal decomposition method, which was adopted from a previous one with a slight modification [23]. In brief, 0.7060 g of $Fe(acac)_3$, 1.012 g of 1, 2-dodecanediol , 2 mL of OA, and 2 mL of OLA were dissolved in 20 mL

of benzyl ether. The mixture was then heated at 65 °C for 15 min under a nitrogen atmosphere. After preheating, the mixture was maintained at 200 °C for 30 min, followed by refluxing under 265 °C for another 30 min. After reaction, the mixture was cooled to ambient temperature. The OA-stabilized SPIO NPs were collected by a magnet, and washed with ethanol for 4 times. The obtained SPIO NPs were then dispersed within TMB solution at a concentration of 1 mg/mL, which was then stored at 4 °C for the following studies.

2.3. Preparation of MPDA@SPIO NPs

MPDA capped SPIO (MPDA@SPIO) NPs were fabricated by a dual-soft-template method. In brief, 30 mg of P123, 75 mg of F127 and 150 mg of dopamine hydrochloride were dissolved in 10 mL of ethanol solution (40%, v/v). The mixture was then mixed with 0.4 mL of SPIO-contained TMB solution, followed by ultrasonication to form SPIO-loaded oil-in-water emulsions. Next, 0.375 mL of $NH_3{\cdot}H_2O$ (28–30%) was immediately added to the reaction systems under continuous stirring. After 4 h of reaction, the MPDA@SPIO NPs were collected by centrifugation, followed by washing with water and ethanol for each 3 times. The obtained products were then dried under a vacuumed condition, which were then stored at 4 °C prior to use.

2.4. Preparation of SAPEG-MPDA@SPIO NPs

For surface modification of MPDA@SPIO NPs with the target molecules of SA, 50 mg of SA-modified polyethylene glycol (SA-PEG-NH_2), which was synthesized by the method as described in our previous study [35], was added to 10 mL of MPDA/SPIO suspensions (1 mg/mL). The mixture was then adjusted to pH 9, followed by stirring for 24 h at ambient temperature. The SA-modified MPDA@SPIO nanoparticles (SAPEG-MPDA@SPIO) were obtained by centrifugation and washing with water for 3 times. MPDA@SPIO nanoparticles without SA modification (PEG-MPDA@SPIO) were also prepared as control groups under the same conditions.

2.5. Preparation of SAPEG-MPDA@SPIO/Fe^{3+} NPs

To prepare SAPEG-MPDA@SPIO/Fe^{3+} NPs, 20 μL of $FeCl_3$ solutions (10 mg/mL) were added into 2 mL of SA-PEG/MPDA/SPIO suspensions (1 mg/mL). After 6 h of storage at 4 °C, the SAPEG-MPDA@SPIO/Fe^{3+} NPs were collected by centrifugation and washing with water for 3 times.

2.6. Physicochemical characterization

The chemical structure of OSA-Fucoidan conjugate was confirmed by ^{1}H NMR spectrometer (AC-80, Bruker Bios pin. Germany). The particle size, size distribution, and zeta-potential of resultant NPs were measured by a dynamic light scattering (DLS) instrument (litesizer 500, Anton-Paar, Austria). The morphologies of NPs were analyzed by a transmission electronic microscopy (TEM; JEM-1200EX, JEOL, Japan) or scanning electronic microscopy (SEM; Hitachi SU-8010, Tokyo, Japan). Fourier transmission infrared (FTIR) spectra of NPs were performed using a FTIR spectroscopy (VECTOR22, Bruker, Germany) in the range from 400 to 4000 cm^{-1}. The ferric content was determined by inductively coupled plasma mass spectrometry (ICP-MS) instrument (NexION300X, PerkinElmer, USA).

2.7. DOX encapsulation and release property

SAPEG-MPDA@SPIO/Fe^{3+} NPs (1 mg) dispersed in 1 mL of PBS solution (5 mM, pH8) was mixed with 1 mL of DOX solution (0–1 mg/mL). The mixture was then continuously stirred for 24 h under a dark condition. The DOX-loaded SAPEG-MPDA@SPIO/Fe^{3+} (named as SAPEG-MPDA@SPIO/DOX/Fe^{3+}) NPs were then obtained by centrifugation and washing with Mill-Q water for 3 times. The DOX content in the supernatant was measured by UV–Vis spectrophotometer (TU-1800PC, Beijing Purkinje General Instrument Co., Ltd., China). The encapsulation efficiency (EE) and drug loading (DL) was calculated according to Eq. (1) and Eq. (2), respectively.

$$EE\% = \frac{\text{Mass of DOX added} - \text{Mass of DOX in the supernatant}}{\text{Mass of DOX added}} \times 100\% \quad (1)$$

$$DL\% = \frac{\text{Mass of DOX in NPs}}{\text{Mass of NPs}} \times 100\% \quad (2)$$

The DOX release behavior from SAPEG-MPDA@SPIO/DOX/Fe^{3+} NPs at pH 7.4 and 5.0 was analyzed by the dialysis bag method. A known amount of SAPEG-MPDA@SPIO/DOX/Fe^{3+} dispersion was transferred into a separate dialysis bag (MWCO 3500), which was then placed in the tubes containing 20 mL of release medium. The tubes were then incubated at 37 °C at a shaking rate of 100 rpm. At a predetermined time, 4 mL of release medium was collected, then the concentration of DOX were determined by UV–vis spectrometry. The released medium was then replaced by the same volume of fresh medium. To investigate the effect of NIR irradiation on the release of DOX, the same amounts of samples were irradiated with 808 nm NIR light (2 W/cm^2, 5 min) at the selected time interval (0, 1, 3, 6 h). The following procedures were the same as the one described above.

2.8. In vitro photothermal experiments

The SAPEG-MPDA@SPIO/Fe^{3+} dispersions at a different concentration (0–1 mg/mL, 200 μL) were placed in 96-well plates, which were then irradiated by 808 nm NIR light at a power density of 2 W/cm^2 for 300 s. The temperature of each sample was recorded every 20 s by a digital thermometer (DT1311, Shenzhen, China). The photothermal stability of SAPEG-MPDA@SPIO/Fe^{3+} NPs (500 μg/mL) were performed by irradiating the samples for 300 s, followed by natural cooling of the temperature for another 900 s for total 4 cycles. The photothermal conversion efficiency of SAPEG-MPDA@SPIO/Fe^{3+} NPs was calculated according to the formulas described in the supplementary information.

2.9. In vitro relaxivity property

In vitro relaxivity property of SAPEG-MPDA@SPIO/Fe^{3+} NPs was performed by a 3.0 T MRI Scanner (Philips Achieva 3.0T TX). The T1 and T2 weight images of SAPEG-MPDA@SPIO/Fe^{3+}, PEG-MPDA@SPIO/Fe^{3+}, and SAPEG-MPDA@SPIO dispersions with different concentration (0–2 mg/mL) were captured, respectively. The T1 relaxation time in term of Fe (adsorbed Fe^{3+}) concentrations was determined by T1-mapping sequence: TR, 290 ms, TE, 15 ms, FOV, 160 × 100, matrix size,160 × 100, slice thickness, 2.0 mm. The T2 relaxation time in term of Fe (Fe content in SPIO) concentrations was determined by T2-mapping sequence: TR, 2000 ms, TE, 56 ms, FOV, 177 × 140, matrix size, 175 × 140, slice thickness, 2.0 mm.

2.10. Cell culture

The human hepatocellular cell line (HepG2 and Bel-7402 cells) and normal liver cell line (LO2 cells) were purchased from the Institute of Biochemistry and Cell Biology of the China Academy of Sciences. Dulbecco's modified eagle medium (DMEM) and fetal bovine serum (FBS) were purchased from Genome Co. Ltd. (Hangzhou, China). HepG2, Bel-7402 and LO2 cells were cultured in DMEM containing FBS (10%), penicillin (100 U/mL), and streptomycin (100 μg/mL) at 37 °C in a humidified atmosphere of 5% CO_2.

2.11. In vitro cellular uptake

The cellular uptake of SAPEG-MPDA@SPIO/DOX/Fe^{3+} and PEG-MPDA@SPIO/DOX/Fe^{3+} NPs was examined on HepG2, Bel-7402 and LO2 cells by a confocal laser scanning microscopy (CLSM; SP8 TCS, Leica, Germany). HepG2, Bel-7402 and LO2 cells (2 mL) were seed separately seeded into 6-well plates at a density of 5×10^5/well. After 24 h of incubation, the medium was replaced with the same volume of fresh medium containing SAPEG-MPDA@SPIO/DOX/Fe^{3+} or PEG-MPDA@SPIO/DOX/Fe^{3+} NPs at a dose of DOX 2.5 μg/mL for another 0.5 and 4 h, respectively. The cells were then washed with PBS, fixed with 4% paraformaldehyde solution, stained with DAPI, and finally analyzed by CLSM observation. The *in vitro* NIR-triggered drug release behavior of SAPEG-MPDA@SPIO/DOX/Fe^{3+} NPs were also investigated. Briefly, HepG2, Bel-7402 and LO2 cells were seeded into 6-well plates containing SAPEG-MPDA@SPIO/DOX/Fe^{3+} for 1 h. After that, the cells were irradiated by an 808 nm NIR laser (2 W/cm^2, 5 min). The cells were allowed for another 3 h of incubation, followed by the CLSM measurements as described above. The corresponding fluorescence signals of each samples were analyzed by image J.

2.12. In vitro cellular MRI

In vitro cellular MRI was performed to further evaluate the feasibility of SAPEG-MPDA@SAPIO/Fe^{3+} NPs for targeted T1/T2 dual-mode MRI application. Briefly, 2 mL of HepG2, Bel-7402 and LO2 cells were seed separately seeded into 6-well plates at a density of 5×10^5/well. After 24 h of incubation, the medium was replaced with the same volume of fresh medium containing 50 μg/mL of SAPEG-MPDA@SAPIO/Fe^{3+} and PEG-MPDA@SAPIO/Fe^{3+} NPs for another 4 h. The cells were then washed with PBS, followed by detaching with trypsin-EDTA. The collected cells were immobilized by 1% agarose, which was then used for T1/T2 dual modal MRI. The T1 and T2 weighted images of the cells were obtained using the same parameters as described in Section 2.9.

2.13. In vitro cytotoxicity

In vitro cytotoxicity of SAPEG-MPDA@SPIO/Fe^{3+} NPs loaded with or without DOX was evaluated on HepG2, Bel-7402 or LO2 cells via MTT assay. Briefly, 200 μL of HepG2, Bel-7402 and LO2 cells were separately seeded into 96-well plates at a density of 5×10^3/well. After 24 h of incubation, 200 μL of fresh medium containing various concentrations of samples (DOX, SAPEG-MPDA@SPIO/DOX/Fe^{3+} and PEG-MPDA@SPIO/DOX/Fe^{3+} NPs) was added into wells after removing the previous medium, and cultured for another 24 h. Twenty microliters of MTT solution (5 mg/mL) was then added into each well, followed by incubation for another 4 h. After incubation, the medium in each well was removed, followed by adding 200 μL of DMSO to dissolve the formazan crystal. Finally, the absorbance at 570 nm was recorded by an automatic reader (Bio-Rad, Model 680, USA). The untreated cells were used as control sample.

To test the chemo-photothermal cytotoxicity, the SAPEG-MPDA@SPIO/Fe^{3+} and SAPEG-MPDA@SPIO/DOX/Fe^{3+}NPs were incubated with HepG2, Bel-7402 and LO2 cells for 4 h. Subsequently, each well was irradiated by an 808 nm NIR light (2 W/cm^2) for 5 min, followed by washing with PBS and culturing with fresh media for another 20 h. Finally, the cell viability was evaluated by the MTT assay as described above.

2.14. Tumor model

Balb/c nude mice were (4–5 weeks, ~16 g) were purchased from Shanghai Silaike Laboratory Animal Co., Ltd. All animal experiments were carried out in accordance with the National Institutes of Health (NIH, USA) guidelines for the care and use of laboratory animals in research. The surgical procedures and experiment protocols were approved by the Committee for Animal Experiments of Zhejiang University. To build the subcutaneous tumor bearing mice model, 5×10^6 HepG2 cells in 100 μL of serum-free DMEM were subcutaneously injected into flank region of each mice. After inoculation, the growth of tumor was closely observed. The tumor volume was calculated as: V = length × width^2/2.

The orthotopic tumor bearing mice model was established by a previously reported method [36]. In brief, a subcutaneous tumor bearing mouse was euthanized by carbon dioxide (CO_2) asphyxiation, and then the tumor tissue was harvested. The tumor tissue was then cut into small pieces (~1 mm^3) in ice-cold DMEM (without FBS) solution before transplantation. Balb/c nude mice were anesthetized by intraperitoneal injection of pentobarbital, then their abdomen was disinfected and prepared for tumor inoculation. A midline laparotomy was performed to expose the normal liver, followed by transplanting the aforementioned HepG2 tumor tissue into the liver parenchyma by using ophthalmic forceps. Hemostasis was performed by compression with hemostatic gelatin sponge for 5 min. After the tumor tissue had been transplanted, stratified incisions were performed with 3.0 F sutures. After two weeks, the successfully established orthotopic tumor bearing mice were used for further study.

2.15. In vivo T1 and T2 dual-mode MRI

For *in vivo* T1/T2 dual-mode MRI, the subcutaneous tumor bearing mice were intravenously injected with SAPEG-MPDA@SPIO/DOX/Fe^{3+} dispersion at DOX dose of 5 mg/kg (3 mice/group). The T1 and T2 weighted images of tumors were before and after treatment for 6 and 24 h were captured by 3.0 T MRI Scanner. The sequence of T1 MRI was: TR, 290 ms, TE, 15 ms, FOV, 70 × 70, matrix size,304 × 201, slice thickness, 2.0 mm. The sequence of T2 MRI was: TR, 3000 ms, TE, 60 ms, FOV, 50 × 50, matrix size, 200 × 176, slice thickness, 2.0 mm.

2.16. In vivo distribution

The evaluation of biodistribution was performed by using both subcutaneous and orthotopic tumor bearing Balb/c nude mice (3 mice/group). The near infrared dye ICG was used to label the NPs (SAPEG-MPDA@SPIO/ICG) before intravenous injection. The method for the preparation of SAPEG-MPDA@SPIO/ICG was described in Supplementary Information. In the case of subcutaneous tumor bearing mice model, the mice were intravenously injected with SAPEG-MPDA@SPIO/ICG or PEG-MPDA@SPIO/ICG at the same ICG dosage (1 mg/kg). After 6 and 24 h post-injection, the mice were anaesthetized, and then their fluorescent photographs were captured by the IVIS Spectrum Imaging System (Caliper, Perkinelmer, USA). In addition, the mice were euthanized by CO_2 asphyxiation at 24 h post-injection, and then their major organs (tumor, heat, liver, spleen, lung and kidney) were collected, which were then imaged to observe the fluorescence signals. In the case of orthotopic tumor bearing mice model, the mice were intravenously injected with SAPEG-MPDA@SPIO/ICG or PEG-MPDA@SPIO/ICG at a dose of ICG 1 mg/kg. At 6 and 24 h post-injection, the major organs (heat, liver, spleen, lung and kidney) were collected, and then imaged by the Maestro system (Cambridge Research & Instrumentation, Inc., Woburn, MA, USA).

2.17. In vivo therapeutic efficacy

The therapeutic efficacy of different treatment was evaluated using subcutaneous HepG2 tumor-bearing mice. After the tumors were reached to 5–6 mm, the mice were randomly divided into 7 groups: (1) PBS; (2) free DOX; (3) PEG-MPDA@SPIO/DOX/Fe^{3+}; (4) SAPEG-MPDA@SPIO/DOX/Fe^{3+}; (5) PBS + NIR; (6) SAPEG-MPDA@SPIO/Fe^{3+} + NIR; (7) SAPEG-MPDA@SPIO/DOX/Fe^{3+} + NIR (n = 5). The mice were intravenously injected with NPs at DOX dose of 5 mg/kg at day 0 and 2, respectively. After 24 h of treatment, the mice were

irradiated with or without 808 NIR light at power density of 2 W/cm^2 for 5 min (1 cm beam diameter). The change in temperature of tumor surface during NIR irradiation was recorded by a digital thermometer (DT1311, Shenzhen, China). At a predetermined time point, the temperature was recorded by putting the probe (2 mm) of the digital thermometer in the middle of surface of the tumor sites. The tumor volume and body weight were recorded every 2 days for total 21 days.

2.18. Histology analysis

The mice were euthanized by CO_2 asphyxiation, and the tumors and major organs (heart, liver, spleen, lung, and kidney) from the treatment groups were collected (3 mice/group), which were then fixed in 4.5% buffered formalin, embedded in paraffin and stained with hematoxylin and eosin (H&E). The morphology of each section was observed by a fluorescence microscope (Olympus, Japan). The tissue slides were examined by Dr. Lu, whom is specialized in pathological analysis.

2.19. Western blotting analysis

The protein was extracted from the HepG2, Bel-7402 and LO2 cells by the RIPA lysis buffer. The concentration of protein in each cell line was then quantified by a bicinchoninic acid assay (Beyotime Biotechnology, Shanghai, China). The protein with an equivalent amount was separated by SDS-PAGE, following by transferring to a PVDF membrane (0.22 μm, Milipore). After blocked for 90 min in blocking buffer at room temperature, the membranes were incubated with the primary antibody anti-(CD62E) overnight at 4 °C. Afterwards, the membranes were incubated with an appropriate secondary antibody for 60 min at room temperature. The target bonds were visualized by an ECL chemiluminescence kit, and GAPDH was used as the control protein.

2.20. Statistical analysis

All data are expressed as the mean ± standard deviation (SD). The difference between groups was performed using one-way analysis of variance (ANOVA) with *post hoc* Tukey tests using SPSS 18.0 (95% confidence interval). P-value of <0.05 was considered as statistically significant difference.

3. Results and discussion

3.1. Preparation of SAPEG-MPDA@SPIO NPs

The fabrication process of SAPEG-MPDA@SPIO NPs was presented in Fig. 1A. SPIO NPs were firstly synthesized by a classical thermal decomposition method using oleic acid as a stabilizer. TEM images and DLS measurements suggested that the SPIO NPs with an average particle size of ~7 nm was narrowly distributed in TMB solution (Figs. 1B and S1). Subsequently, sialic acid-grafted PEG (SA-PEG-NH_2) was synthesized according to the procedures described in our previous study [35]. ^{1}H-NMR examination was performed to confirm the structure of the prepared SA-PEG-NH_2. It was found that the spectra of SA-PEG-NH_2 had the characteristic peaks at 2.01 and 3.58 belonged to SA (-CH_3) and NH_2-PEG-NH_2 (-O-CH_2CH_2-), respectively (Fig. S2). This observation suggested that SA-PEG-NH_2 was successfully synthesized in our current

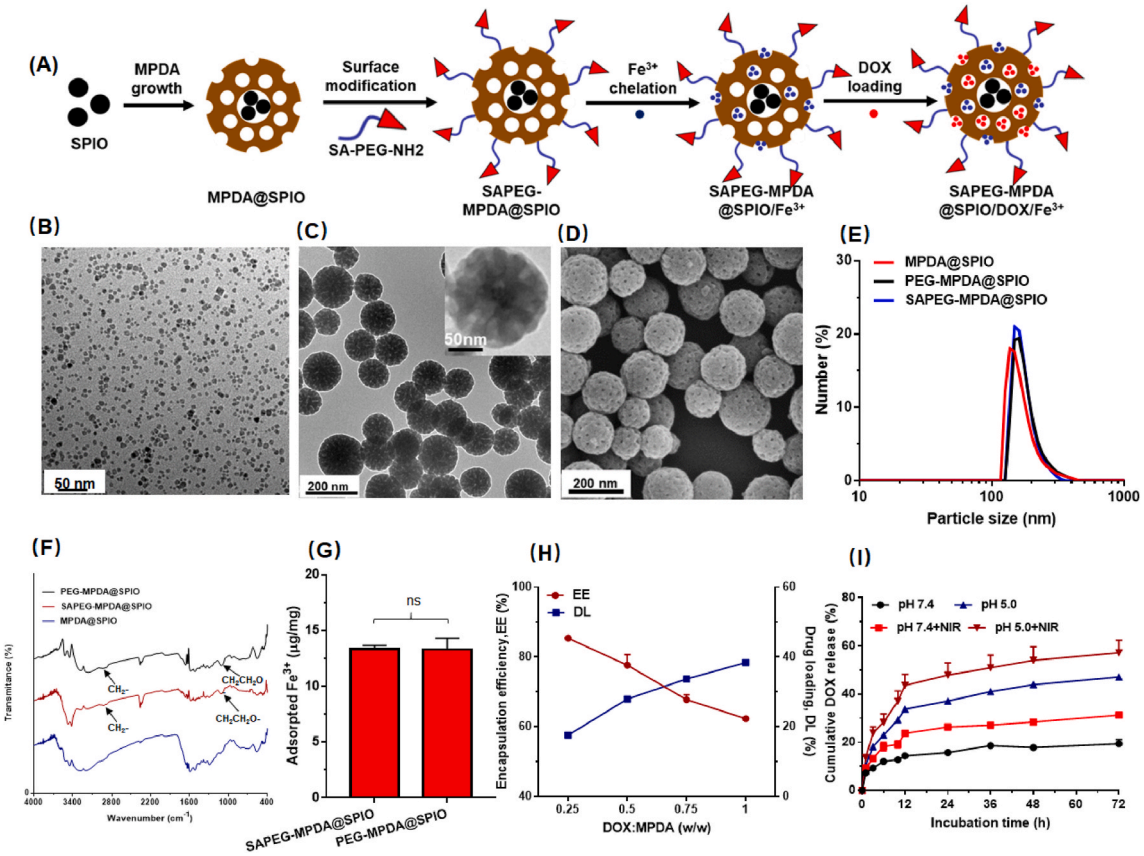

Fig. 1. Preparation and characterization of SAPEG-MPDA@SPIO/DOX/Fe^{3+} NPs. (A) Schematic illustration of the preparation of SAPEG-MPDA@SPIO/DOX/Fe^{3+} NPs. (B) TEM images of SPIO NPs. (C) TEM images of SAPEG-MPDA@SPIO NPs. (D) SEM images of SAPEG-MPDA@SPIO NPs. Particle size distribution (E) and FTIR spectra (F) of MPDA@SPIO, PEG-MPDA@SPIO and SAPEG-MPDA@SPIO NPs. (G) The amount of Fe^{3+} chelated by PEG-MPDA@SPIO NPs and SAPEG-MPDA@SPIO NPs. (H) The DOX encapsulation efficiency (EE) and drug loading capability (DL) of SAPEG-MPDA@SPIO/Fe^{3+} NPs. (I) The DOX release profiles of SAPEG-MPDA@SPIO/DOX/Fe^{3+} NPs. (ns is non-significant, n = 3).

work.

After that, a dual-soft-template method was used to the prepare MPDA@SPIO NPs. To improve the stability and endow the tumor-targeting ability, MPDA@SPIO NPs functionalized with SA-PEG-NH_2 (SAPEG-MPDA@SPIO) were prepared by simply mixing MPDA@SPIO dispersions with SA-PEG-NH_2 under mild alkaline condition. Typical TEM and SEM images revealed that the prepared SAPEG-MPDA@SPIO NPs composed of spherical particles with an average diameter of around 155 nm (Fig. 1C and D). A close examination of SAPEG-MPDA@SPIO NPs suggested that the SPIO NPs were incorporated within the MPDA@SPIO NPs, which had well-defined mesoporous structures (Fig. 1C). DLS results further confirmed that the SAPEG-MPDA@SPIO NPs had a narrow particle distribution with an average diameter of 167.6 ± 12.8 nm (Fig. 1E and Table S1). In addition, we found that the MPDA@SPIO, SAPEG-MPDA@SPIO and PEG-MPDA@SPIO NPs had similar particle sizes and size distributions, suggesting that the PEGylation had little impact on the size of MPDA@SPIO NPs (Fig. 1E).

FTIR and stability examinations were performed to investigate whether or not the MPDA@SPIO NPs was bound with SA-PEG-NH_2 or CH_3-PEG-NH_2. As shown in Fig. 1F, both of SAPEG-MPDA@SPIO and PEG-MPDA@SPIO NPs had the characteristic bands at 2865 and 1080 cm^{-1}, which belonged to the stretch vibration of C–H and C–O in the alkyl chain of PEG, respectively (Fig. 1F). In addition, it was found that MPDA@SPIO NPs were severely aggregated after storage in PBS solution overnight, whereas PEGylated MPDA@SPIO NPs were physical stable without evidences of agglomeration (Fig. S3). The aforementioned results indicated that CH_3-PEG-NH_2 or SA-PEG-NH_2 was successfully grafted onto the surfaces of MPDA@SPIO NPs. It is well acknowledged that PDA-based materials could be easily surface modified by amino-terminated or thiol-terminated polymers via the Schiff/Michael reaction [25,37].

3.2. Ferric ion chelation

To complex with paramagnetic Fe^{3+} ions, SAPEG-MPDA@SPIO NPs were simply mixed with $FeCl_3$ solution without the assistance of any extrinsic chelators. After removing the unabsorbed Fe^{3+}, the obtained Fe^{3+}-chelated SAPEG-MPDA@SPIO (SAPEG-MPDA@SPIO/Fe^{3+}) NPs showed spherical shapes with average particle size of ~180 nm (Table S1). ICP-MS measurements showed that the amount of Fe^{3+} adsorbed by SAPEG-MPDA@SPIO and PEG-MPDA@SPIO NPs was not significantly different, which was 13.38 ± 0.29 and 13.31 ± 1.01 μg/mg, respectively (Fig. 1G). The amount of Fe $^{3+}$ chelated by MPDA NPs prepared in our study was much higher than that of nonporous PDA even with smaller particle size (7.2–8.6 μg of Fe^{3+} per mg of PDA NPs) as reported in previous studies [25,38]. The successful chelation of Fe^{3+} by SAPEG-MPDA@SPIO NPs was further proved by the pronounced change of zeta potential from −31.6 ± 3.7 to −15.7 ± 2.4 mV (Table S1). Similar tendency was also observed for the Fe^{3+}-chelated PEG-MPDA@SPIO NPs. In addition, DLS and SEM data indicated that the chelation of Fe^{3+} had little changes on the morphology and particle size of the PEGylated MPDA@SPIO NPs (Fig. S4 and Table S1).

3.3. DOX loading and release property

The encapsulation of DOX by SAPEG-MPDA@SPIO/Fe^{3+} NPs was prepared by simply mixing the chemotherapy drug with the SAPEG-MPDA@SPIO/Fe^{3+} NPs in PBS solution for 24 h. As shown in Fig. 1H, the encapsulation of DOX was decreased with increasing the ratio of DOX to MPDA, whereas the loading capability of DOX displayed an opposite trend. The increased drug loading capability was attributed to the increase in weight ratio of feeding DOX and MPDA. It was also found that the average particle size of SAPEG-MPDA@SPIO/DOX/$Fe^{3+}$was increased as the feeding ratio of DOX to MPDA was increased, whereas the corresponding PDI were maintained at relatively low values of ~0.2 (Fig. S5A). Similar behavior of PDA-based drug delivery system was also reported in other previous study [37]. In addition, the encapsulation efficiency, drug loading capability, average particle size and PDI values quite similar between SAPEG-MPDA@SPIO/DOX/Fe^{3+} and PEG-MPDA@SPIO/DOX/Fe^{3+} NPs prepared by feeding the same ratio of DOX and MPDA, demonstrating that the modification of targeted SA had little impact on the preparation of DOX-loaded MPDA NPs (Figures S5A, S5B and S5C). Taking encapsulation ratio, drug loading content, particle size, and potential combined effect of chemotherapy and PTT, SAPEG-MPDA@SPIO/DOX/Fe^{3+} with drug feeding ratio of 0.25 were used for the following studies.

The drug release behavior of SAPEG-MPDA@SPIO/DOX/Fe^{3+} NPs was analyzed by the dialysis method. According to Fig. 1I, the SAPEG-MPDA@SPIO/DOX/Fe^{3+} NPs showed a sustained DOX release during 72 h of incubation under pH 7.4 and 5.0, respectively. However, the release rate of DOX at pH 5.0 was much quicker than that of PH 7.4. This behavior was related to the protonation of amine group in DOX in an acidic environment, leading to a disruption of π-π and hydrophobic interactions between MPDA and DOX, finally resulting in an accelerated release of DOX from MPDA NPs [39]. The photothermal influence on the release of DOX was also investigated by exposing the SAPEG-MPDA@SPIO/DOX/Fe^{3+} dispersion under an 808 nm NIR light at power density of 2 W/cm^2 for 5min. As shown in Fig. 1I, the release of DOX from SAPEG-MPDA@SPIO/DOX/Fe^{3+} NPs at pH 5.0 and pH 7.4 were both accelerated by the irradiation of NIR light. The NIR-triggered DOX release was possibly attributed to two reasons: (i) the movement of nanoparticles was largely enhanced by NIR irradiation, (ii) the π–π conjugation between DOX and MPDA might be weakened by the heat energy produced by NIR irradiation [40]. It is noteworthy that the delivery systems with dual pH- and thermal-triggered drug release behavior provides the chemotherapy drugs with considerably lower side effects by the regulation of intracellular drug release [41].

3.4. In vitro photothermal properties

In vitro photothermal experiments were firstly conducted by investigating the changes in the temperature of aqueous solution containing different concentrations of SAPEG-MPDA@SPIO/Fe^{3+} NPs under NIR irradiation (2.0 W cm^{-2}, 300 s). The SAPEG-MPDA@SPIO/Fe^{3+} dispersions showed a striking increase of temperature after the NIR irradiation, following a concentration- and time-dependent manner (Fig. 2A). The temperature of SAPEG-MPDA@SPIO/Fe^{3+} dispersions even could be increased to ~70 °C at a concentration of 500 μg/mL, whereas the water showed little change of temperature at the same irradiation condition. This observation demonstrated that SAPEG-MPDA@SPIO/Fe^{3+} NPs had a great NIR light-induced thermal ability.

The photothermal performance of SAPEG-MPDA@SPIO/Fe^{3+} NPs (500 μg/mL) was also highly dependent on the NIR energy density, with a higher energy density resulting in a higher and rapider increase of temperature (Fig. 2B). In addition, SAPEG-MPDA@SPIO/Fe^{3+} dispersions showed non-significant changes of photothermal performances during 4 cycles of NIR irradiation at 2.0 W cm^{-2}, suggesting their excellent photothermal stability (Fig. 2C). According to Fig. 2D and E, the photothermal conversion efficiency of SAPEG-MPDA@SPIO/Fe^{3+} NPs was calculated to be 36.2%, which is much higher than those of gold nanorods (27.1%), CuS NPs (27.2%), and graphene oxide-based NPs (13.9%) reported in previous studies [42–44]. Overall, the obtained results in this part demonstrated that SAPEG-MPDA@SPIO/Fe^{3+} NPs possessed excellent photothermal conversion capability and photostability, which could be served as a promising candidate for PTT applications.

3.5. Relaxivity measurements

To evaluate whether SAPEG-MPDA@SPIO/Fe^{3+} NPs could be used as a potential T1/T2 dual-mode MRI contrast agent, their T1 and T2

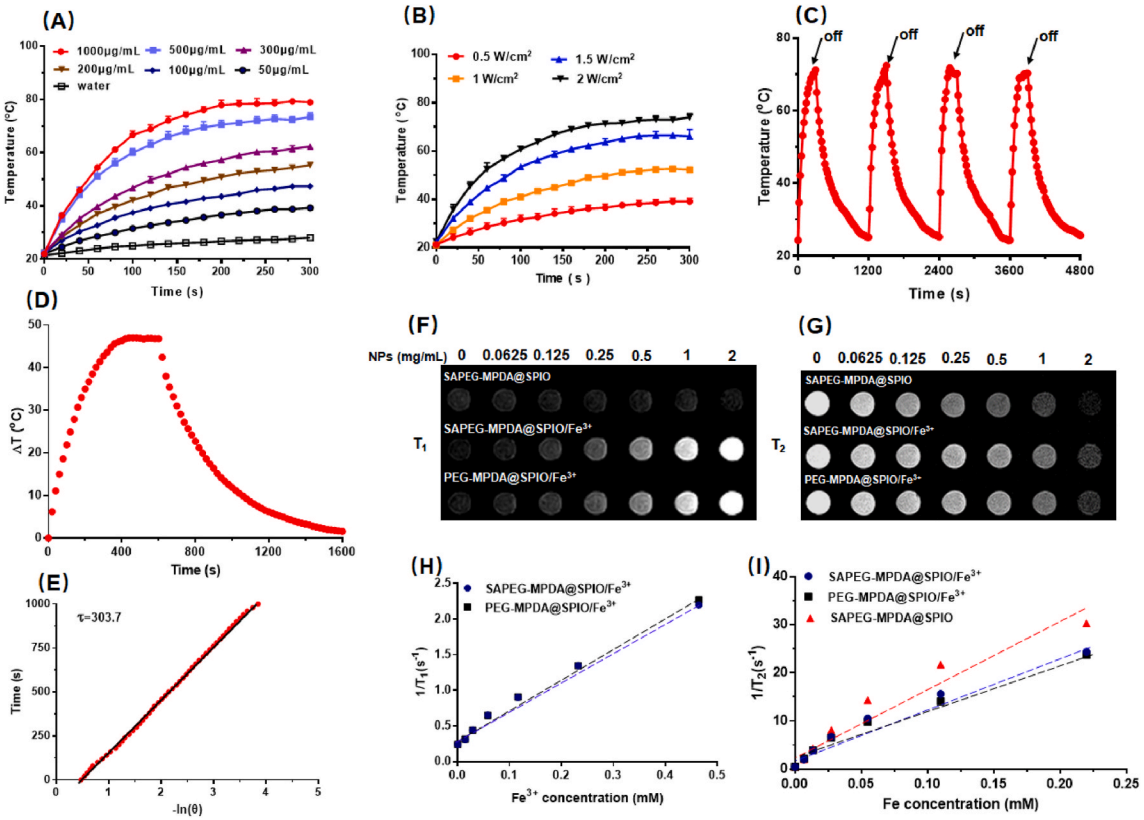

Fig. 2. *In vitro* photothermal and relaxivity properties. (A) The changes in the temperature of SAPEG-MPDA@SPIO/Fe^{3+} dispersions with different concentration under NIR irradiation (2 W/cm^2, 300s). (B) The changes in the temperature of SAPEG-MPDA@SPIO/Fe^{3+} (500 μg/mL) dispersions under NIR irradiation with different power density. (C) Photostability of SAPEG-MPDA@SPIO/Fe^{3+} (500 g/mL) under NIR irradiation (2 W/cm^2) for 4 cycles. (D) Photothermal effect of the aqueous dispersion of MPDA@SPIO/Fe^{3+} (500 μg/mL) for 1600 s. (E) Linear time date versus-lnθ obtained from the cooling period. The T1 weighted images (F) and T2 weighted images (G) of SAPEG-MPDA@SPIO/Fe^{3+}dispersions at different concentrations. The T1 relaxation rates (H) and T2 relaxation rates (I) of SAPEG-MPDA@SPIO/Fe^{3+}dispersions at different concentrations.

weighted images were captured by 3.0 T MRI. The resultant data revealed that the increase of SAPEG-MPDA@SPIO/Fe^{3+} NPs concentration resulted in brighter T1 weighted images and darker T2 weighted images, respectively (Fig. 2F and G). Similar results were also observed for the PEG-MPDA@SPIO/Fe^{3+} NPs. In contrast, the increase of SAPEG-MPDA@SPIO NPs concentration only resulted in darker T2 weighted images, suggesting that the Fe^{3+}-free MPDA@SPIO almost had no T1 posit ive contrast enhancement effect. The r_1 relaxivity value of SAPEG-MPDA@SPIO/Fe^{3+} NPs was calculated to be 4.29 ± 0.14 $mM^{-1}s^{-1}$ in term of chelated Fe^{3+} concentration (Fig. 2H). This value is quite similar to that of Gd-DTPA (3.56–4.96 $mM^{-1}s^{-1}$) as published in previous studies [36,45,46]. The r_2 relaxivity value of SAPEG-MPDA@SPIO/Fe^{3+} NPs was calculated to be 105.53 ± 1.86 $mM^{-1}s^{-1}$ in term of Fe concentration, which was calculated from the content of SPIO (Fig. 2I). Similar r_1 and r_2 relaxivity values were also observed for PEG-MPDA@SPIO/Fe^{3+} NPs (Fig. 2H and I). By contrast, the r_2 relaxivity value of SAPEG-MPDA@SPIO NPs was 135.60 $mM^{-1}s^{-1}$, which was higher than that of SAPEG-MPDA@SPIO/Fe^{3+} and PEG-MPDA@SPIO/Fe^{3+} NPs. The relatively reduced r_2 relaxivity value of PEGylated MPDA chelated with Fe^{3+} could be attributed to the interference effects between these two different contrast agents [47]. Overall, these results revealed that SAPEG-MPDA@SPIO/Fe^{3+} NPs could be a potent candidate for T1/T2 dual-model MRI imaging.

3.6. Cellular uptake

The cellular uptake of SAPEG-MPDA@SPIO/DOX/Fe^{3+} and PEG-MPDA@SPIO/DOX/Fe^{3+} NPs by HepG2, Bel-7402 and LO2 cells were investigated by CLSM method. As shown in Fig. 3A, all of the samples displayed a time-dependent cellular uptake, with a prolonged time (4 h) leading to a higher fluorescence intensity than a shorter incubation time (0.5 h). In addition, at the same incubation time, the HepG2 and Bel-7402 cells treated with SAPEG-MPDA@SPIO/DOX/Fe^{3+} NPs showed a significantly stronger fluorescence intensity than those of the other groups (Fig. 3A and B). It was well known that E-selectin is highly upregulated on the surfaces of cancer cells, such as HepG2 and Bel-7402 cells [30,31]. Western blotting analysis was also performed in our study, which further confirmed that the expression levels of E-selectin in HepG2 and Bel-7402 cells was much higher than that of LO2 cells (Fig. S6). On the other hand, the targeted molecule of SA has specific ability to bind with E-selectin, which is well established by many previous studies [35,48]. The enhanced cellular uptake of SAPEG-MPDA@SPIO/DOX/Fe^{3+} NPs by HepG2 and Bel-7402 cells was therefore closely related to its E-selectin targeting ability generated by the SA modification.The photothermal influence on the cellular uptake of SAPEG-MPDA@SPIO/DOX/Fe^{3+} NPs was also investigated. The results suggested that the NIR irradiation endowed the SAPEG-MPDA@SPIO/DOX/Fe^{3+} NPs with a significant enhanced cellular uptake by the three cell lines, as evidenced by a stronger fluorescence intensity was observed in the NIR irradiated cells in comparison with those without NIR irradiation (Fig. 3A and C). The enhanced internalization of SAPEG-MPDA@SPIO/DOX/Fe^{3+} NPs by NIR irradiation was ascribed to two possible mechanisms: (i) the NIR irradiation accelerated the release of DOX from the NPs, thereby resulting in a stronger fluorescence intensity in the cells [49]; (ii) the mild photothermal heat promoted membrane permeability, which was also account for the enhanced internalization of SAPEG-MPDA@SPIO/DOX/Fe^{3+} NPs [50,51]. Overall, these results indicated that the

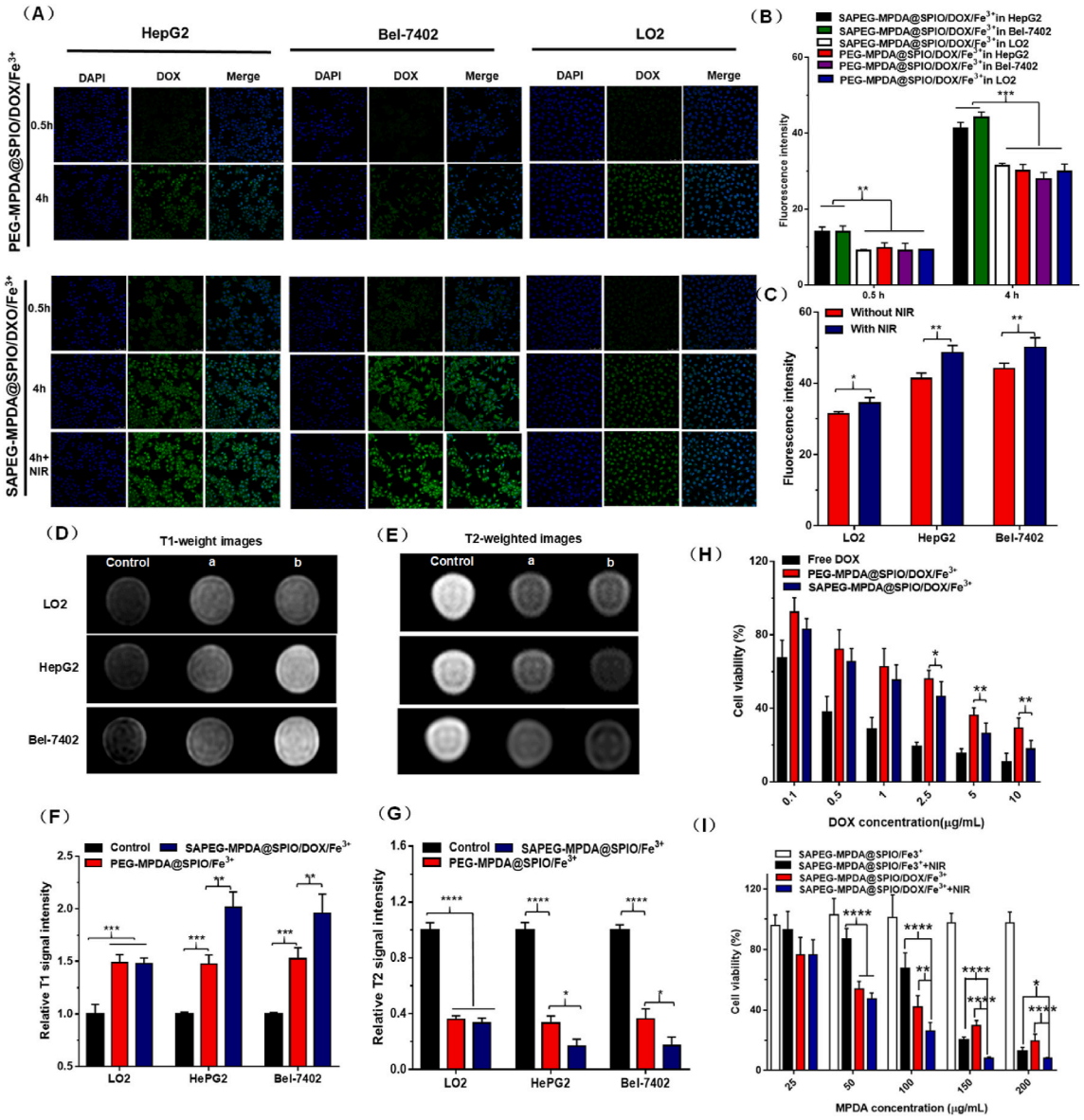

Fig. 3. *In vitro* cellular studies. (A) Confocal fluorescence images of HepG2, Bel-7402 and LO2 cells incubated with SAPEG-MPDA@SPIO/DOX/Fe^{3+} and PEG-MPDA@SPIO/DOX/Fe^{3+} for 0.5 and 4 h, respectively. Scale bar = 75 μm. (B) The fluorescence intensity of HepG2, Bel-7402 and LO2 cells treated with SAPEG-MPDA@SPIO/DOX/Fe^{3+} or PEG-MPDA@SPIO/DOX/Fe^{3+} NPs for 0.5 and 4, respectively. (C) Effect of NIR irradiation on the change of fluorescence intensity of HepG2, Bel-7402 and LO2 cells treated with SAPEG-MPDA@SPIO/DOX/Fe^{3+}NPs. The T1 weighted image (D) and relatively T1 MR signal intensity (F) of HepG2, Bel-7402 and LO2 cells incubated with SAPEG-MPDA@SPIO/Fe^{3+} and PEG-MPDA@SPIO/Fe^{3+} NPs for 4 h, respectively. The T2-weighted image (E) and relatively T2 MR signal intensity (G) of HepG2, Bel-7402and LO2 cells incubated with SAPEG-MPDA@SPIO/Fe^{3+} and PEG-MPDA@SPIO/Fe^{3+} NPs for 4 h, respectively. Control is the cells without any treatment, (a) is the cells treated with PEG-MPDA@SPIO/Fe^{3+}, and (b) is cells treated with SAPEG-MPDA@SPIO/Fe^{3+} NPs. (H) Cell viability of HepG2 cells treated with free DOX, SAPEG-MPDA@SPIO/DOX/Fe^{3+} and PEG-MPDA@SPIO/DOX/Fe^{3+} NPs at different DOX dosage. (I) Cell viability of HepG2 cells incubated with various concentrations of SAPEG-MPDA@SPIO/DOX/Fe^{3+} NPs with or without NIR irradiation. (*P < 0.05, **P < 0.01, ***P < 0.001, ****P < 0.0001, n = 3).

SAPEG-MPDA@SPIO/DOX/Fe^{3+} NPs could be effectively internalized by the hepatic cancer cells and the release of DOX could be triggered by the NIR light.

3.7. *In vitro targeted T1 and T2 dual-mode MRI*

The T1 and T2 weighted images of HepG2, Bel-7402 and LO2 cells treated with SAPEG-MPDA@SPIO/Fe^{3+}NPs for 4 h were obtained to further confirm the targeting ability of SA-functionalized MPDA@SPIO. As compared with the control group, the HepG2, Bel-7402 and LO2 cells treated with SAPEG-MPDA@SPIO/Fe^{3+} or PEG-MPDA@SPIO/Fe^{3+}NPs both exhibited a brighter signal on T1 weighted MR images, but a darker signal on T2 weighted MR images (Fig. 3D and E). It should be noted that the HepG2 and Bel-7402 cells treated with SAPEG-MPDA@SPIO/Fe^{3+} had a significantly larger increase in relative T1 MR signal intensity and decrease in relative T2 MR signal intensity than the other groups (Fig. 3F and G). Those results further validated the T1 and T2 dual mode MRI performance of SAPEG-MPDA@SPIO/DOX/Fe^{3+}, and its targeting ability towards hepatic cancer cells was attributed to the presence of SA on the surfaces of MPDA@SPIO.

3.8. *Cytotoxicity evaluation*

First of all, the cytotoxicity of SAPEG-MPDA@SPIO/Fe^{3+} and PEG-

MPDA@SPIO/Fe^{3+} NPs towards HepG2, Bel-7402 and LO2 cells was evaluated by MTT assay. Apparently, both of SAPEG-MPDA@SPIO/Fe^{3+} and PEG-MPDA@SPIO/Fe^{3+} NPs were nontoxic towards the three cell lines, with cell viabilities being >90% at tested concentration up to 150 μg/mL, revealing their excellent biocompatibility (Figures S7A, S7B and S7C).*In vitro* therapeutic effect of SAPEG-MPDA@SPIO/DOX/Fe^{3+} and PEG-MPDA@SPIO/DOX/Fe^{3+} NPs was then assessed. According to Fig. 3H, S8A and S8B, all of the tested samples showed a dose-dependent cytotoxicity, with a higher DOX dosage resulting in a higher ability to kill the cells. Apparently, the cytotoxicity of free DOX is much higher than that of SAPEG-MPDA@SPIO/DOX/Fe^{3+} or PEG-MPDA@SPIO/DOX/Fe^{3+} NPs at the same DOX concentration, which was possibly due to that free DOX had a quicker drug release than that of the other two preparations. It was also found that the hepatic cancer cells (HepG2 and

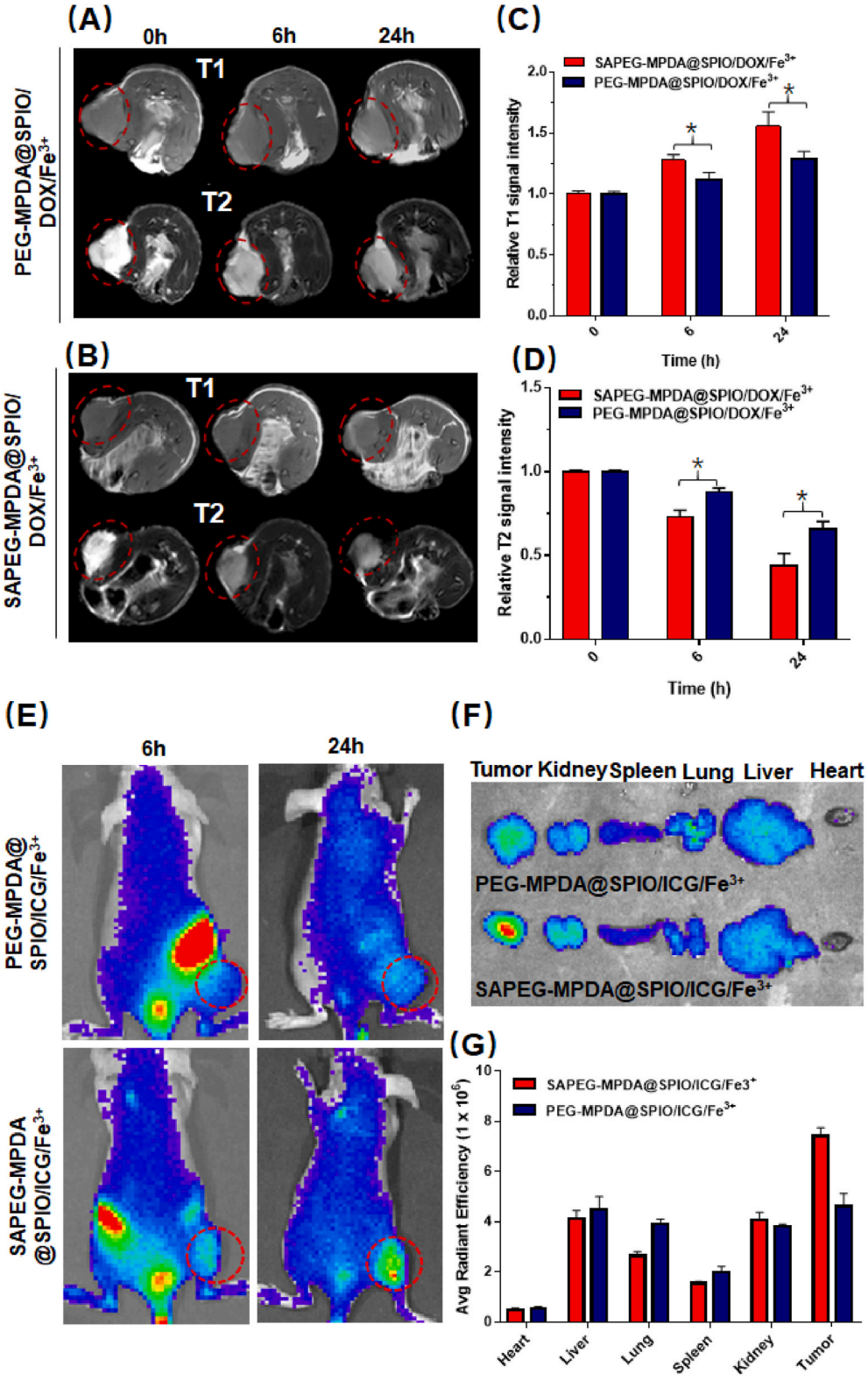

Fig. 4. *In vivo* MRI and distribution. *In vivo* T1 weighted images (A) and relative T1 MRI signal intensity (C) of tumors following the administration of SAPEG-MPDA@SPIO/DOX/Fe^{3+} and PEG-MPDA@SPIO/DOX/Fe^{3+} NPs at different time points. *In vivo* T2 weighted images (B) and relative T2 MRI signal intensity (D) of tumors following the administration of SAPEG-MPDA@SPIO/DOX/Fe^{3+} and PEG-MPDA@SPIO/DOX/Fe^{3+} NPs at different time points. (E) The fluorescence images of HepG2-bearing mice treated with SAPEG-MPDA@SPIO/ICG/Fe^{3+} and PEG-MPDA@SPIO/ICG/Fe^{3+} at different time point. The fluorescence images (F) and fluorescence intensity (G) of harvested tissue at 24 h post-injection. (*P < 0.05, n = 3).

Bel-7402 cells) incubated with SAPEG-MPDA@SPIO/DOX/Fe^{3+} had significantly lower cell viabilities than those incubated with PEG-MPDA@SPIO/DOX/Fe^{3+} at the same DOX concentration. Due to the high affinity between SA and E-selectin, SAPEG-MPDA@SPIO/DOX/Fe^{3+} had the ability to internalize into the hepatic cancer cells via a E-selectin receptor-mediated endocytosis pathway, thereby resulting in a higher cytotoxicity than PEG-MPDA@SPIO/DOX/Fe^{3+}. However, in the case of LO2 cells, the DOX-loaded nanoparticles showed a similar cytotoxicity at the same DOX concentration, independent of whether or not the nanoparticles were modified with SA. Different from the hepatic cancer cells, the LO2 cells expressed few levels of E-selectin, thus they had no the E-selectin receptor-mediated endocytosis pathway to effectively internalize the SAPEG-MPDA@SPIO/DOX/Fe^{3+}. These results further confirmed that SAPEG-MPDA@SPIO/DOX/Fe^{3+} had the ability to target the hepatic cancer cells.The photothermal influence on the cytotoxicity of SAPEG-MPDA@SPIO/DOX/Fe^{3+} NPs was also investigated by exposing the cells under an 808 NIR light at power density of 2 W/cm^2 for 5min. As shown in Fig. 3I and Fig. S8C**,** the HepG2 and Bel-7402 cells treated with SAPEG-MPDA@SPIO/Fe^{3+} NPs at concentration of $\leq$50 μg/mL were hardly died under NIR irradiation, suggesting the limited PTT effects produced at this condition. Thus, the inhibition of cellular growth was mainly dependent on the chemotherapeutic drug at a relatively low dosage of SAPEG-MPDA@SPIO/DOX/Fe^{3+} NPs. The PTT efficacy was largely enhanced with increasing the concentration of SAPEG-MPDA@SPIO/Fe^{3+} NPs from 50 to 200 μg/mL, as reflected by its better ability to kill the cells at a higher dosage. On the other hand, the NIR irradiation could significantly improve the ability of SAPEG-MPDA@SPIO/DOX/Fe^{3+} NPs to kill the cells at a relative high concentration, as reflected by its lowest cell viability compared with the other groups, which was due to the combined treatment of chemotherapy and PTT. Similar behaviors were also observed in the chemo-photothermal cytotoxicity towards LO2 cells (Fig. S8D). Overall, *in vitro* studies suggested that suggested that both of cancer cells and normal cells could be killed by the treatment of chemotherapy or PTT. Thus, it is extremely important to develop nanodrugs with considerably higher accumulation into tumor sites than the normal tissues, which could significantly reduce the side effects and improve the therapeutic outcomes.

3.9. *In vivo targeted T1 and T2 dual-mode MRI*

In vivo MRI performances were conducted to determine whether SAPEG-MPDA@SPIO/DOX/Fe^{3+} NPs could be used as a targeted T1 and T2 weighted MRI contrast agent. Fig. 4A and B revealed the T1 and T2 weighted images of tumor before injection, and 6 h and 24 h post injection, respectively. As compared with images of tumor before injection, a significant T1 positive and T2 negative contrast enhancement was observed at the MR images of tumor sites treated with NPs. The enhancement effect showed a time-dependent manner, with 24 h post injection resulting in a large increase of T1 signal intensity and decrease of T2 signal intensity than 6 h post injection (Fig. 4C and D**)**, which is possibly due to that a larger amount of NPs entered into the tumor sites with a prolonged time. We also found that the T1 positive and T2 negative contrast enhancement caused by injection with SAPEG-MPDA@SPIO/DOX/Fe^{3+} NPs was more significant than that of PEG-MPDA@SPIO/DOX/Fe^{3+} NPs at the same time, which was possibly due to active targeting ability of SAPEG-MPDA@SPIO/DOX/Fe^{3+} NPs. Overall, these results demonstrated that SAPEG-MPDA@SPIO/DOX/Fe^{3+} NPs have hepatic tumor targeting ability, which could largely improve the imaging effect of liver cancer.

3.10. *In vivo biodistribution*

In vivo biodistribution experiment was also performed to further confirm the targeting ability of SAPEG-MPDA@SPIO/Fe^{3+} NPs. The near infrared dye ICG was used to label the SAPEG-MPDA@SPIO/Fe^{3+}(SAPEG-MPDA@SPIO/ICG/Fe^{3+}) before administration. Apparently, a prolonged time led to a higher accumulation of SAPEG-MPDA@SPIO/ICG/Fe^{3+} or PEG-MPDA@SPIO/ICG/Fe^{3+} NPs in the subcutaneous tumor sites, since the fluorescent intensity of tumor region at 6 h post injection was lower than that of 24 h post injection (Fig. 4E). In addition, at 24 h post-injection, the accumulation of SAPEG-MPDA@SPIO/ICG/Fe^{3+} NPs in tumors was much higher than that of PEG-MPDA@SPIO/ICG/Fe^{3+} NPs, as evidenced by the considerably stronger fluorescent intensity (Fig. 4F and G). These results suggested that SA modification and a relatively longer blood circulation time could effectively enhance the accumulation of MPDA-based NPs into the tumor sites, which was consistent with the results obtained from *in vivo* MRI study.

In vivo biodistribution examination was also carried out in the orthotopic tumor bearing mice model (Figs. S9A and S9B). It was found that the PEG-MPDA@SPIO/ICG/Fe^{3+} NPs were mainly accumulated in the normal liver tissues at 6 h post-injection. In comparison, the liver tumor regions of mice treated with SAPEG-MPDA@SPIO/ICG/Fe^{3+} NPs showed a significant higher fluorescence intensity than that of the normal liver tissues, indicating that SAPEG-MPDA@SPIO/ICG/Fe^{3+} NPs could actively target to hepatic tumor sites. In addition, the result also demonstrated that the amount of these two nanoparticles accumulated in normal liver tissues were considerably decreased at 24 h post-injection. This behavior could be closely associated with that the injected nanoparticles were eliminated by Kupffer cells present in the normal liver tissues [52].

Overall, *in vivo* studies based on the subcutaneous and orthotopic tumor bearing mice models both revealed the active delivery of SAPEG-MPDA@SPIO/ICG/Fe^{3+}NPs towards tumor sites, which was possibly due to the specific bind of SA with the E-selectin upregulated in the tumor tissues. This behavior was extremely important for the nanomedicines, which could effectively minimize the side effects and improve the therapeutic effects for cancer therapy.

3.11. *In vivo antitumor effect*

To evaluate the anticancer efficacy *in vivo*, the HepG2 tumor-bearing Balb/c nude mice were divided into 7 groups for different treatments. Before evaluation, the changes in the temperature of tumor sites treated with PBS, SAPEG-MPDA@SPIO/DOX/Fe^{3+} or SAPEG-MPDA@SPIO/Fe^{3+} NPs were monitored to investigate whether they could produce *in vivo* PTT under NIR irradiation or not. The results suggested that the administration of SAPEG-MPDA@SPIO/DOX/Fe^{3+} NPs significantly increased the temperature from 36.5 to 52.4 °C after 5 min of irradiation at power density of 2 W/cm^2 **(**Fig. 5A). Similar tendency was also observed in the tumor sites treated with SAPEG-MPDA@SPIO/Fe^{3+} NPs. However, the surface temperature of tumor sites treated with PBS only increased by ~5 °C under the same irradiation condition. Previous study has shown that the cancer cells could survive when the temperature is lower than 43 °C, whereas they are hardly alive at a temperature higher than 49 °C [53]. Thus, we believed that the treatment of SAPEG-MPDA@SPIO/DOX/Fe^{3+} or SAPEG-MPDA@SPIO/Fe^{3+} NPs could provide *in vivo* PTT activity under NIR irradiation.

As shown in Fig. 5C, only the mice treated with free DOX showed an obvious decline of body weight during the first 7 days of treatments. This phenomenon was also reported in the previous studies, which was due to the side effect of free DOX [31,54]. However, there was a clear difference on the changes of tumor volumes between groups with different treatments (Fig. 5B). For the PBS and PBS+NIR groups, there was a quick increase of tumor volume within 21 days, suggesting that only NIR irradiation had little effect on the inhibition of tumor growth, which was due to the limited enhanced temperature. In comparison, the mice treated SAPEG-MPDA@SPIO/Fe^{3+} NPs under NIR irradiation showed a much slower growth rate of tumor volumes, which was due to the PTT effect produced by MPDA. We also found that the mice treated with free DOX, PEG-MPDA@SPIO/DOX/Fe^{3+} or SAPEG-MPDA@SPIO/DOX/Fe^{3+} NPs showed a significant delay in tumor growth, where

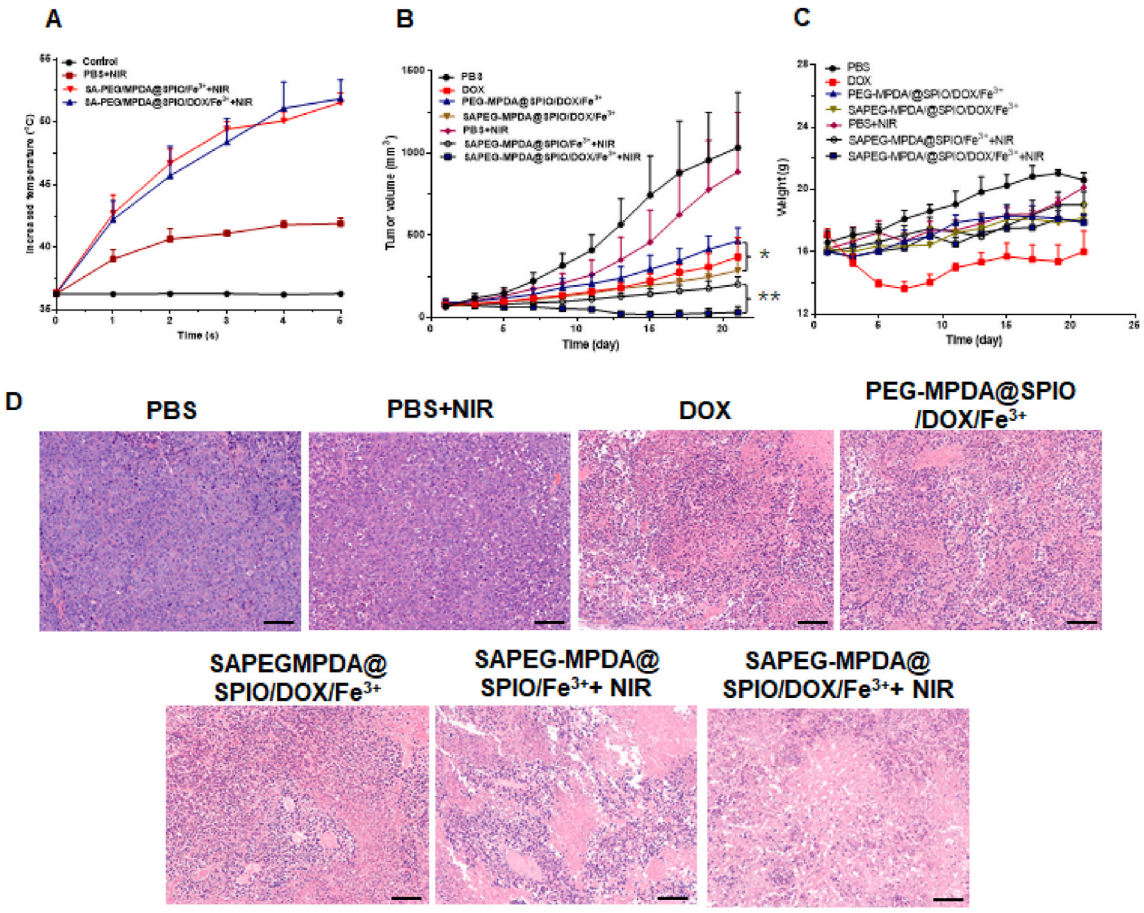

Fig. 5. *In vivo* antitumor effect. (A) The temperature changes against time in tumor surface of mice exposed to 808 nm NIR light for 5 min, where the control group was the HepG2 tumor-bearing mice without NIR irradiation. The changes of tumor volume (B) and body weight (C) of HepG2 tumor-bearing mice with different treatment. (D) H&E stained images of tumor tissues collected from mice in different treatment groups. Scale bar = 100 μm. (*P < 0.05, **P < 0.01, n = 5).

SAPEG-MPDA@SPIO/DOX/Fe^{3+} NPs had a better therapeutic effect than the other two groups. The enhanced anticancer ability of SAPEG-MPDA@SPIO/DOX/Fe^{3+} NPs was possibly due to the sustained DOX release from NPs and the active targeting in the tumor region via SA modification [31,55]. Notably, the mice treated with SAPEG-MPDA@SPIO/DOX/Fe^{3+} NPs and NIR irradiation showed significantly restrained tumor growth compared with the other groups, which was due to the combined effect between chemotherapy and PTT.

H&E stained images of tumor tissues were also captured to confirm the therapeutic effects of different treatments (Fig. 5D). Apparently, most of tumor cells were destroyed in SAPEG-MPDA@SPIO/DOX/Fe^{3+}+ NIR irradiation groups, further confirming the combined chemo-photothermal therapy could lead to an enhanced treatment of hepatic cancer. There were several reasons accounting for the enhanced anticancer efficacy of the combined chemo-photothermal therapy [40,56,57]: (i) The released DOX can stabilize the topoisomerase II complex after it breaks the DNA chain for replication, preventing the DNA double helix from being resealed, and thereby stopping the replication process of tumor cells; (ii) PTT can directly kill the cancer cells via the produced heat, but also improve the cellular uptake by facilitating the cell membrane permeability; (iii) PTT could trigger the DOX release, thereby further enhancing the chemotherapeutic effect; (iv) PTT also has an ability to modulate the tumor microenvironments by suppressing the macrophages polarization towards the M2 pro-tumor phenotype.

H&E stained images of major organs were also obtained to evaluate the biosafety of various treatment (Fig. 6). Histopathological changes of major organ from the treatment group were not obvious compared to the control group, indicating the negligible long-term adverse toxicity towards the major organs. Although, previous study has reported that free DOX could lead to liver and heart damages [4]. The slight damage on liver and heart tissue caused free DOX in this study was possibly due to the relatively short administration period [58].

4. Conclusions

In summary, we have fabricated SAPEG-MPDA@SPIO/DOX/Fe^{3+} NPs as a new theranostic agent for T1/T2 dual modal MRI-guided chemo-photothermal treatment of liver cancer. It was found that SAPEG-MPDA@SPIO chelated with Fe^{3+} had excellent T1 positive and T2 negative contrast enhancement effect, but also showed excellent photothermal conversion ability and stability. The chemotherapy drug of DOX could be effectively loaded within SAPEG-MPDA@SPIO/Fe^{3+} via π-π stacking, which showed pH/NIR dual-responsive release behaviors. *In vitro* and *in vivo* studies had revealed that SAPEG-MPDA@SPIO/DOX/Fe^{3+} NPs could be highly uptake by the hepatic cancer cells and accumulated in tumor region, which was due to the specific binding of SA with the overexpressed E-selectin. This properites also endowed the SAPEG-MPDA@SPIO/DOX/Fe^{3+} NPs with the ability to track the distribution of NPs via T1/T2 dual modal MRI. Futhurmore, SAPEG-MPDA@SPIO/DOX/Fe^{3+} NPs were effective at inhibiting the tumor growth under NIR irradiation due to the combined effect of chemotherapy and PTT. Overall, our study has demonstrated that the SAPEG-MPDA@SPIO/DOX/Fe^{3+} NPs is a promising candidate for T1/T2 dual modal MRI-guided targeted chemo-photothermal therapy for hepatic cancer. It could also provide useful information for the development of theranostic agents that were used for the treatment of

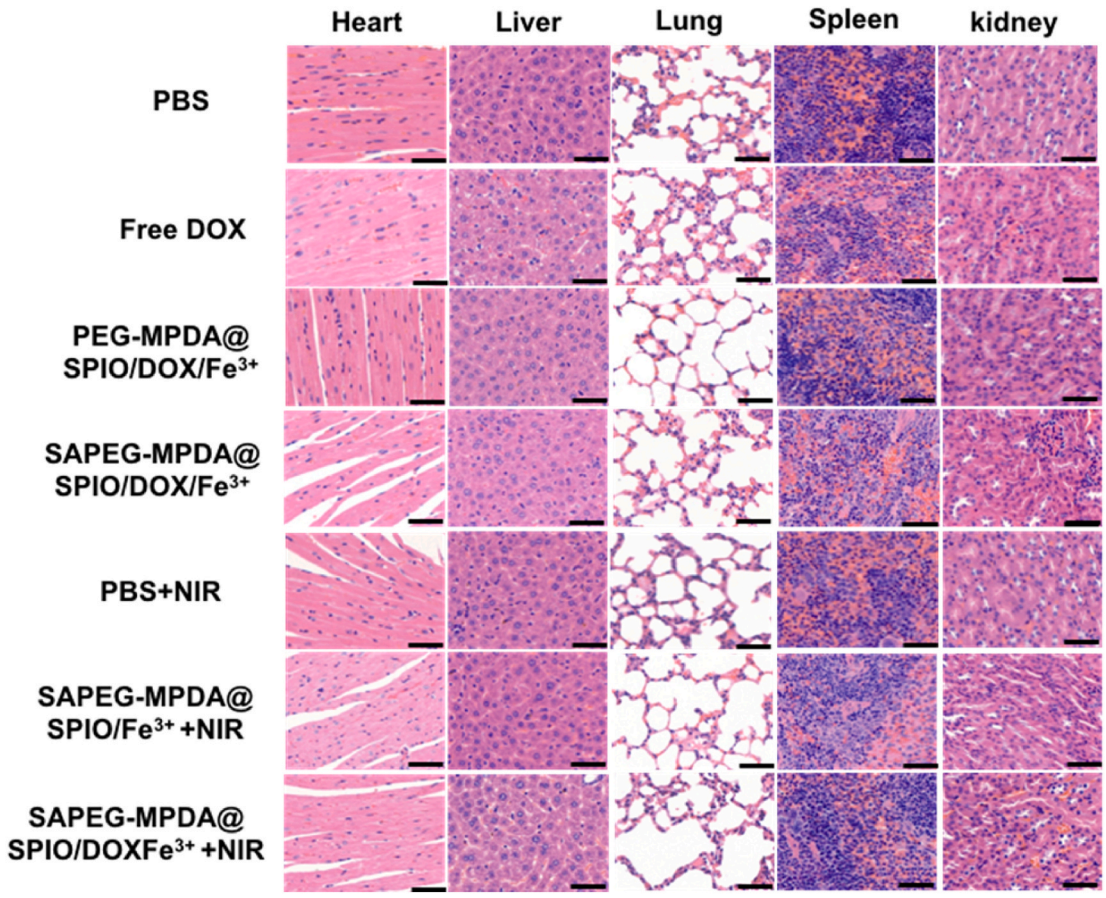

Fig. 6. *In vivo* toxicity evaluation: Representative H&E stained images of major organs collected from mice with different treatments. Scale bar = 50 μm.

different cancers. However, there are still many other furture studies (such as the optimal preparation method for large-scale production, clinical studies, and so on) should be carried out before the clinical application of this novel theranostic agent.

CRediT authorship contribution statement

Gaofeng Shu: Conceptualization, Investigation, Methodology, Validation, Writing - original draft. **Minjiang Chen:** Conceptualization, Investigation, Methodology, Validation. **Jingjing Song:** Conceptualization, Investigation, Methodology, Validation. **Xiaoling Xu:** Investigation, Methodology. **Chenying Lu:** Investigation, Methodology. **Yuyin Du:** Validation, Conceptualization, Funding acquisition, Supervision, Writing - review & editing, Jiansong Ji, Conceptualization, Funding acquisition, Supervision, Writing - review & editing. **Min Xu:** Investigation, Methodology. **Zhongwei Zhao:** Investigation, Methodology. **Minxia Zhu:** Investigation, Methodology. **Kai Fan:** Validation. **Shiji Fang:** Validation. **Bufu Tang:** Validation.

Declaration of competing interest

The authors declare that they have no known competing financial interests or personal relationships that could have appeared to influence the work reported in this paper.

Acknowledgements

This work was supported by Institute of Nanomaterials and Nanotechnology, Lishui Hospital of Zhejiang University; Postdoctoral Foundation of ZheJiang province; National Key Research and Development projects intergovernmental cooperation in science and technology of China (2018YFE0126900); Zhejiang Provincial Natural Science Foundation (LY15H030010, LY20H180016, Q21H180011). The Key R&D Program of Lishui City (2019ZDYF17).

Appendix A. Supplementary data

Supplementary data to this article can be found online at https://doi.org/10.1016/j.bioactmat.2020.10.020.

References

[1] M. Sherman, et al., Screening for hepatocellular carcinoma: the rationale for the American association for the study of liver diseases recommendations, Hepatology 56 (3) (2012) 793–796.
[2] X.-P. Zhang, et al., A nomogram to predict early postoperative recurrence of hepatocellular carcinoma with portal vein tumour thrombus after R0 liver resection: a large-scale, multicenter study, Eur. J. Surg. Oncol. 45 (9) (2019) 1644–1651.
[3] Qiying, et al., Paclitaxel/hydroxypropyl-β-cyclodextrin complex-loaded liposomes for overcoming multidrug resistance in cancer chemotherapy, J. Liposome Res. 30 (1) (2019) 12–20.
[4] N.N. Zhang, et al., Visual targeted therapy of hepatic cancer using homing peptide modified calcium phosphate nanoparticles loading doxorubicin guided by T1 weighted MRI, Nanomed. Nanotechnol. Biol. Med. 14 (7) (2018) 2167–2178.
[5] L. Gao, et al., Tumor-penetrating peptide conjugated and doxorubicin loaded T1-T2 dual mode MRI contrast agents nanoparticles for tumor theranostics, Theranostics 8 (1) (2018) 92–108.
[6] E.K. Lim, et al., Nanomaterials for theranostics: recent advances and future challenges, Chem. Rev. 115 (1) (2015) 327–394.
[7] E. Terreno, et al., Challenges for molecular magnetic resonance imaging, Chem. Rev. 110 (5) (2010) 3019–3042.
[8] T.-H. Shin, et al., Recent advances in magnetic nanoparticle-based multi-modal imaging, Chem. Soc. Rev. 44 (14) (2015) 4501–4516.
[9] Y. Chen, et al., Multifunctional envelope-type mesoporous silica nanoparticles for pH-responsive drug delivery and magnetic resonance imaging, Biomaterials 60 (2015) 111–120.

[10] P. Verwilst, et al., Recent advances in Gd-chelate based bimodal optical/MRI contrast agents, Chem. Soc. Rev. 44 (7) (2015) 1791–1806.
[11] D. Liu, et al., Effective PEGylation of iron oxide nanoparticles for high performance in vivo cancer imaging, Adv. Funct. Mater. 21 (8) (2011) 1498–1504.
[12] L. Ren, et al., MRI-guided liposomes for targeted tandem chemotherapy and therapeutic response prediction, Acta Biomater. 35 (2016) 260–268.
[13] S.P. Lin, J.J. Brown, MR contrast agents: physical and pharmacologic basics, J. Magn. Reson. Imag.: Off. J. Int. Soc. Magn. Reson. Med. 25 (5) (2007) 884–899.
[14] P. Padmanabhan, et al., Nanoparticles in practice for molecular-imaging applications: an overview, Acta Biomater. 41 (2016) 1–16.
[15] C. Lu, et al., Hydroxyl–PEG–Phosphonic acid stabilized superparamagnetic manganese oxide-doped iron oxide nanoparticles with synergistic effects for dual mode MR imaging, Langmuir 35 (2019) 9474–9482.
[16] F. Hu, Y.S. Zhao, Inorganic nanoparticle-based T 1 and T 1/T 2 magnetic resonance contrast probes, Nanoscale 4 (20) (2012) 6235–6243.
[17] D. Li, et al., Biomimetic albumin-modified gold nanorods for photothermo-chemotherapy and macrophage polarization modulation, Acta Pharm. Sin. B 8 (1) (2018) 74–84.
[18] S. Shen, et al., Targeting mesoporous silica-encapsulated gold nanorods for chemo-photothermal therapy with near-infrared radiation, Biomaterials 34 (12) (2013) 3150–3158.
[19] Q. Tian, et al., Hydrophilic flower-like CuS superstructures as an efficient 980 nm laser-driven photothermal agent for ablation of cancer cells, Adv. Mater. 23 (31) (2011) 3542–3547.
[20] K. Yang, et al., Nano-Graphene in biomedicine: theranostic applications, Chem. Soc. Rev. 42 (2) (2013) 530–547.
[21] Y. Xia, et al., Gold nanocages: from synthesis to theranostic applications, Acc. Chem. Res. 44 (10) (2011) 914–924.
[22] Yanlan, et al., Dopamine-melanin colloidal nanospheres: an efficient near-infrared photothermal therapeutic agent for in vivo cancer therapy, Adv. Mater. 25 (9) (2013) 1353–1359.
[23] R. Ge, et al., Fe3O4@ polydopamine composite theranostic superparticles employing preassembled Fe3O4 nanoparticles as the core, ACS Appl. Mater. Interfaces 8 (35) (2016) 22942–22952.
[24] Z.-H. Miao, et al., Intrinsically Mn2+-chelated polydopamine nanoparticles for simultaneous magnetic resonance imaging and photothermal ablation of cancer cells, ACS Appl. Mater. Interfaces 7 (31) (2015) 16946–16952.
[25] D. Hu, et al., Indocyanine green–loaded polydopamine–iron ions coordination nanoparticles for photoacoustic/magnetic resonance dual-modal imaging-guided cancer photothermal therapy, Nanoscale 8 (39) (2016) 17150–17158.
[26] Y. Chen, et al., Polydopamine-based coordination nanocomplex for T1/T2 dual mode magnetic resonance imaging-guided chemo-photothermal synergistic therapy, Biomaterials 77 (2016) 198–206.
[27] Y. Xing, et al., Mesoporous polydopamine nanoparticles with co-delivery function for overcoming multidrug resistance via synergistic chemo-photothermal therapy, Nanoscale 9 (25) (2017) 8781–8790.
[28] L. Zhang, et al., Multifunctional mesoporous polydopamine with hydrophobic paclitaxel for photoacoustic imaging-guided chemo-photothermal synergistic therapy, Int. J. Nanomed. 14 (2019) 8647–8663.
[29] N. Kamaly, et al., Targeted polymeric therapeutic nanoparticles: design, development and clinical translation, Chem. Soc. Rev. 41 (7) (2012) 2971–3010.
[30] C.W. Jung, et al., Characterization of hepatocellular carcinoma cell lines based on cell adhesion molecules, Int. J. Mol. Med. 29 (6) (2012) 1158–1164.
[31] Zhu, et al., Sialic-acid-anchored micelles: a hierarchical targeting device for enhanced tumor tissue accumulation and cellular internalization, Mol. Pharm. 15 (9) (2018) 4235–4246.
[32] X.-L. Xu, et al., Endogenous sialic acid-engineered micelles: a multifunctional platform for on-demand methotrexate delivery and bone repair of rheumatoid arthritis, Nanoscale 10 (6) (2018) 2923–2935.
[33] J.B. Hu, et al., E-selectin-targeted sialic acid-PEG-dexamethasone micelles for enhanced anti-inflammatory efficacy for acute kidney injury, Theranostics 7 (8) (2017) 2204–2219.
[34] X.-L. Xu, et al., Highly integrated nanoplatform based on an E-Selectin-targeting strategy for metastatic breast cancer treatment, Mol. Pharm. 16 (8) (2019) 3694–3702.
[35] X.-L. Xu, et al., Sialic acid-functionalized pH-triggered micelles for enhanced tumor tissue accumulation and active cellular internalization of orthotopic hepatocarcinoma, ACS Appl. Mater. Interfaces 10 (38) (2018) 31903–31914.
[36] N.-n. Zhang, et al., Gadolinium-loaded calcium phosphate nanoparticles for magnetic resonance imaging of orthotopic hepatocarcinoma and primary hepatocellular carcinoma, Biomater. Sci. 8 (7) (2020) 1961–1972.
[37] H. Wu, et al., Hydroxyethyl starch stabilized polydopamine nanoparticles for cancer chemotherapy, Chem. Eng. J. 349 (2018) 129–145.
[38] K.-Y. Ju, et al., Bio-inspired, melanin-like nanoparticles as a highly efficient contrast agent for T1-weighted magnetic resonance imaging, Biomacromolecules 14 (10) (2013) 3491–3497.
[39] X. Wang, et al., Multi-responsive photothermal-chemotherapy with drug-loaded melanin-like nanoparticles for synergetic tumor ablation, Biomaterials 81 (2016) 114–124.
[40] L. Qiang, et al., A novel macrophage-mediated biomimetic delivery system with NIR-triggered release for prostate cancer therapy, J. Nanobiotechnol. 17 (1) (2019) 83.
[41] X. Mu, et al., EGFR-targeted delivery of DOX-loaded Fe3O4@ polydopamine multifunctional nanocomposites for MRI and antitumor chemo-photothermal therapy, Int. J. Nanomed. 12 (2017) 2899–2911.
[42] S. Wang, et al., Core-satellite polydopamine-gadolinium-metallofullerene nanotheranostics for multimodal imaging guided combination cancertherapy, Adv. Mater. 29 (35) (2017), 1701013.
[43] N.Q. Zhou, et al., Extracellular biosynthesis of copper sulfide nanoparticles by Shewanella oneidensis MR-1 as a photothermal agent, Enzym. Microb. Technol. 95 (2016) 230–235.
[44] Z. Li, et al., Enhancing the photothermal conversion efficiency of graphene oxide by doping with NaYF 4 : Yb, Er upconverting luminescent nanocomposites, Mater. Res. Bull. 106 (2018) 365–370.
[45] J. Cai, et al., A transferrin-target magnetic/fluorescent dual-mode probe significantly enhances the diagnosis of non-small cell lung cancer, Oncotarget 7 (26) (2016) 40047–40059.
[46] XingDing, et al., Polydopamine coated manganese oxide nanoparticles with ultrahigh relaxivity as nanotheranostic agents for magnetic resonance imaging guided synergetic chemo-/photothermal therapy, Chem. Sci. 7 (11) (2016) 6695–6700.
[47] K. Cheng, et al., Hybrid nanotrimers for dual T 1 and T 2-weighted magnetic resonance imaging, ACS Nano 8 (10) (2014) 9884–9896.
[48] H. Liu, et al., Sialic acid-modified dexamethasone lipid calcium phosphate gel core nanoparticles for target treatment of kidney injury, Biomater. Sci. 8 (14) (2020) 3871–3884.
[49] Manjie, et al., Precise synthesis of unique polydopamine/mesoporous calcium phosphate hollow Janus nanoparticles for imaging-guided chemo-photothermal synergistic therapy, Chem. Sci. 8 (12) (2017) 8067–8077.
[50] Z. Li, et al., Multifunctional bismuth selenide nanocomposites for anti-tumor thermo-chemotherapy and imaging, ACS Nano 10 (1) (2016) 984–997.
[51] T. Zheng, et al., Gold-Nanosponge-based multistimuli-responsive drug vehicles for targeted chemo-photothermal therapy, Adv. Mater. 28 (37) (2016) 8218–8226.
[52] E. Sadauskas, et al., Kupffer cells are central in the removal of nanoparticles from the organism, Part. Fibre Toxicol. 4 (1) (2007) 1–7.
[53] Y. Zhang, et al., Temperature-dependent cell death patterns induced by functionalized gold nanoparticle photothermal therapy in melanoma cells, Sci. Rep. 8 (1) (2018) 8720.
[54] J.-Q. Situ, et al., Multifunctional SPIO/DOX-loaded A54 homing peptide functionalized dextran-g-PLGA micelles for tumor therapy and MR imaging, Sci. Rep. 6 (2016) 35910.
[55] H. Liu, et al., Multifunctional gold nanoshells on silica nanorattles: a platform for the combination of photothermal therapy and chemotherapy with low systemic toxicity, Angew. Chem. Int. Ed. 50 (4) (2011) 891–895.
[56] X. Deng, et al., Polarization and function of tumor-associated macrophages mediate graphene oxide-induced photothermal cancer therapy, J. Photochem. Photobiol. B Biol. 208 (2020), 111913.
[57] H. Zhu, et al., Doxorubicin redox biology: redox cycling, topoisomerase inhibition, and oxidative stress, Reactive oxygen species (Apex, NC) 1 (3) (2016) 189–198.
[58] Y. Octavia, et al., Doxorubicin-induced cardiomyopathy: from molecular mechanisms to therapeutic strategies, J. Mol. Cell. Cardiol. 52 (6) (2012) 1213–1225.